

See discussions, stats, and author profiles for this publication at: <https://www.researchgate.net/publication/221968541>

Coupled Electron Transfer and Proton Hopping in the Final Step of CYP19–Catalyzed Androgen Aromatization

ARTICLE *in* BIOCHEMISTRY · MARCH 2012

Impact Factor: 3.02 · DOI: 10.1021/bi300017p · Source: PubMed

CITATIONS

23

READS

42

2 AUTHORS:



Kakali Sen

Max Planck Institute for Coal Research

14 PUBLICATIONS 122 CITATIONS

[SEE PROFILE](#)



John C Hackett

Virginia Commonwealth University

27 PUBLICATIONS 681 CITATIONS

[SEE PROFILE](#)



NIH Public Access

Author Manuscript

Biochemistry. Author manuscript; available in PMC 2013 April 10.

Published in final edited form as:

Biochemistry. 2012 April 10; 51(14): 3039–3049. doi:10.1021/bi300017p.

Coupled electron transfer and proton hopping in the final step of CYP19-catalyzed androgen aromatization[†]

Kakali Sen[‡] and John C Hackett*

Institute for Structural Biology and Drug Discovery and School of Pharmacy, Virginia Commonwealth University, Richmond, Virginia 23219

Abstract

Aromatase (CYP19) catalyzes the terminal step in estrogen biosynthesis, which requires three separate oxidation reactions, culminating in an enigmatic aromatization that converts an androgen to an estrogen. A stable ferric peroxy ($\text{Fe}^{3+}\text{O}_2^{2-}$) intermediate is seen by electron paramagnetic resonance but its role in this complex reaction remains controversial. Combining molecular dynamics simulation and hybrid quantum mechanics/molecular mechanics, we show that ferric peroxy addition to the 19-aldehyde initiates the reaction. Stepwise cleavage of the C10-C19 and O-O bonds of the peroxohemiacetal extrudes formate and yields Compound II, which in turn desaturates the steroid through successive abstraction of the 1 β -hydrogen atom and deprotonation of the 2 β -position. Throughout the transformation, a proton is cyclically relayed between D309 and the substrate to stabilize reaction intermediates. This mechanism invokes novel oxygen intermediates and provides a unifying interpretation of past experimental mechanistic studies.

Keywords

Aromatase; Cytochrome P450; Quantum Mechanics/Molecular Mechanics; Electron Transfer; Ferric Peroxy; Aromatase; Molecular Dynamics Simulation

The cytochromes P450 (CYPs)1 are among the most diverse enzymatic catalysts, using O_2 and two electrons to oxidize a myriad of substrates. The CYPs that cleave C-C bonds are possibly the most mechanistically flexible of such enzymes; however, the pathways and reactive intermediates of this group remain poorly understood.(1, 2) Aromatase (CYP19) is a prototypical example of the C-C cleaving CYPs. This enzyme has drawn considerable interest for its ability to construct an aromatic ring and for its success as a breast cancer therapeutic target.(3) CYP19 catalyzes a distributive, three-step oxidative transformation of androstenedione (AD) to estrone (ES).(4) The first two steps are accepted to be

[†]This work was supported by grants awarded to J.C.H from the National Institutes of Health (GM092827) and the American Cancer Society.

*Corresponding Author: John C Hackett, Virginia Biotech I, Suite 212, 800 East Leigh St. Richmond, Virginia, USA 23219. Telephone: +1.804.828.5679, Fax: +1.804.827.3664, jchackett@vcu.edu.

[‡]Current Address: Theoretical Chemistry, Max-Planck-Institut für Kohlenforschung, Kaiser-Wilhelm-Platz 1, D-45470 Mülheim an der Ruhr, Germany

Supporting Information Available. Cartesian coordinates of atoms in the QM layer, absolute energies, complete references, and population analyses. This material is available free of charge via the Internet at <http://pubs.acs.org>.

¹**Abbreviations:** Androstenedione, AD; Aromatase, CYP19; Cytochromes P450, CYP; Canonical ensemble, NVT; Compound I, Cpd I; Compound II, Cpd II; Conjugate gradient, CG; Estrone, ES; Ferric peroxy, $\text{Fe}^{3+}\text{O}_2^{2-}$; Ferric peroxy tetramesitylporphyrin, [$\text{Fe}^{3+}(\text{TMP})\text{O}_2^{2-}$]; Isobaric-isothermal ensemble, NPT; Intermediate, I; Molecular dynamics, MD; 19-Oxoandrostenedione, 19-oxoAD; Peroxohemiacetal, PH; Protonated Intermediate, PI; Protonated peroxohemiacetal, HPH; Protonated transition state, HTS; Quantum mechanics/Molecular Mechanics, QM/MM; Reduced Nicotinamide Adenine Dinucleotide Phosphate, NADPH; Transition state, TS.

hydroxylations, while the final step proceeds by an enigmatic mechanism that deforms 19-oxoAD, cleaves the C10-C19 bond (CC hereafter), and aromatizes the steroid.(5) (Scheme 1) Experiments with isotopically-labeled substrates indicate the 1 β - and 2 β -hydrogens are removed and integrated into H₂O, while oxygen atoms from the first and third steps are incorporated into formate. (5–11)

A number of experimental studies support that the ferric peroxy (Fe³⁺O₂²⁻) mediates the third step of the CYP19 reaction. In a model of the enzyme-catalyzed aromatization reaction, Wertz and coworkers demonstrated that a truncated AD analogue is aromatized by a Fe³⁺O₂²⁻ porphyrin complex, [Fe³⁺(TMP)O₂²⁻].(12) More recently, it has been demonstrated that non-heme Fe³⁺O₂²⁻ complexes deformylate aldehydes; while the corresponding hydroperoxy species do not.(13, 14) In contrast to wild-type cytochrome P450cam where Fe³⁺O₂²⁻ has been elusive due to rapid protonation even at cryogenic temperatures,(15) electron paramagnetic resonance of radiolytically-reduced oxyferrous CYP19 revealed accumulation of Fe³⁺O₂²⁻.(16) These observations indicate that there are unique features of the CYP19 active site that increase the stability of this species relative to standards of CYP reactivity. Nevertheless, the precise role of Fe³⁺O₂²⁻ in the final step has remained a controversial mechanistic question in CYP enzymology.

To provide mechanistic insight into this unusual reaction and promote cooperation with experiment, we turned to theory to explore paths of Fe³⁺O₂²⁻ initiated 19-oxoAD aromatization. Using the recent crystal structure of CYP19(17), these studies were performed in the context of the complete protein environment using molecular dynamics (MD) and hybrid quantum mechanics/molecular mechanics (QM/MM) simulations.

Computational Methodology

System Preparation and MD Simulation

The initial coordinates for CYP19 with androstenedione (AD) bound were taken from the crystal structure of human placental aromatase (PDB ID: 3EQM).(17) AD was replaced by 19-oxoAD and O₂ was added manually. The propKa module of the PDB2PQR suite of programs(18–20) and visual inspection of local side chain environments were used to adjust the protonation states of ionizable residues to be consistent with pH 7.0. With the exception of D309, acidic residues were deprotonated (negatively charged), while arginine and lysine residues were protonated (positively charged). Histidine residues were doubly protonated (109, 111, 171, 459, 475), singly protonated at N δ (105, 128, 325, 402, 480), or singly protonated at N ϵ (62). The final charge of the polypeptide was +10. Molecular mechanics parameters for the iron protoporphyrin IX and O₂ were taken from the CHARMM22 force field.(21) Missing parameters for the heme/CysS⁻ were from Bathelt(22) and Oda et. al. (23) The molecular mechanics parameters for 19-oxoAD were taken from previously calculated parameters for biologically important steroids by Cournia (24) and our previous extension for the lanosterol-14-carboxaldehyde.(25) Additional parameters for 19-oxoAD were calculated using two model systems; one comprising the A/B rings and the other the C/D rings of AD. The geometries of these models were fully optimized at the B3LYP/6-31G* level of theory. In turn, additional parameters were generated from automated frequency matching(26) to the B3LYP/6-31G* harmonic vibrational frequencies. Electrostatic potential charges were derived using the CHELPG scheme. (27) Dihedral parameters were derived from relaxed potential energy surface scans of 3-butene-2-one. The resulting topology and requisite CHARMM parameters for 19-oxoAD are provided in the Supporting Information.

Oxyferrous CYP19 with 19-oxoAD in the active site was solvated on all sides with a 15 Å layer of TIP3P water. Electroneutrality and an ionic strength (0.15 M) in the simulation

system was established by adding 26 Na⁺ and 34 Cl⁻ ions. Explicit solvent MD simulations were performed using NAMD 2.7(28) and the CHARMM22(21) force field. All the simulations were performed using Langevin dynamics with periodic boundary conditions at 300 K. In NPT simulations, pressure was maintained with the Langevin piston method. Long-range electrostatics were treated with the Particle Mesh Ewald method. The system was initially subjected to 5000 steps of conjugate gradient (CG) minimization to eliminate any unphysical contacts. Next, water and ions were equilibrated in the NVT ensemble for 200 ps while keeping the protein, oxyheme and 19-oxoAD fixed. This was followed by 5000 steps of CG minimization and 200 ps equilibration in the NPT ensemble with the protein backbone harmonically restrained (5 kcal · mol⁻¹ · Å⁻²). With the protein appropriately solvated, subsequent simulations were carried out with decreasing restraints to enforce sampling of conformations where 19-oxoAD remains in a catalytically competent orientation in the active site. First, a 10 ns simulation was performed with restraints (20 kcal · mol⁻¹ · Å⁻²) between O_p-1βH, O_d-C19, and the 3-keto O-D309. Second, the simulation was continued with the 3-keto O-D309 harmonic restraint removed. Third, the simulation was continued for a final 20 ns run in the absence of harmonic restraints.

Partitioning of QM and MM systems

Coordinates of the CYP19 protein, associated ligands, and a 7 Å bounding water shell were extracted from MD trajectory points, resulting in systems of greater than 19,000 atoms for QM/MM treatment. These systems were subjected to 16,000 geometry optimization steps using CHARMM 31b1. Optimized systems were partitioned into a region for QM treatment containing the O₂-coordinated porphyrin, the C437 side chain (methylthiolate unit), D309 side chain (acetate unit), and the substrate A/B rings. Propionate, methyl, and vinyl side chains of the heme as well as the atoms of C and D ring of the substrate were excluded. Atoms within 7 Å of the QM region remained unrestrained during QM/MM geometry optimizations, while the remaining atoms were frozen.

QM/MM Methodology

QM/MM calculations were performed with the ChemShell(29) package, which integrates the TURBOMOLE(30) and DL-POLY(31) packages for density functional theory and MM calculations, respectively. The electrostatic embedding scheme with the charge shift correction was used to represent the electrostatic interaction between the QM region and the surrounding partial charge distribution.(32) No electrostatic cutoff was used in the QM/MM calculations. In QM/MM geometry optimizations, the QM region was treated with the B3LYP density functional(33, 34) and the Ahlrichs VTZ basis set for Fe, 6-31+G* for N, O, S and the 6-31G* basis sets for C, H. The CHARMM22(21) force field was used for the MM region. Stationary points were subject to single point energy calculations with the B3LYP and PBE0(35–37) density functionals, Wachter's+f basis set(38) for Fe, and TZVP basis set for the remaining atoms. Basis sets for geometry optimizations and single-point energy calculations are denoted B1 and B2 in the text, respectively. Unless otherwise noted, the discussion is limited to the energetics derived from UB3LYP/B1:CHARMM calculations to focus on key results. These were subsequently verified by single-point calculations with larger basis sets (B2) and the PBE0 density functional. Transition states were verified by the presence of single imaginary frequency along the reaction coordinate using the numerical vibrational analysis tool in ChemShell. In cases when transition state geometry optimizations failed to converge, reported energetic barriers were derived from relaxed potential energy surface scans. Since there are a few cases where relative energetics are derived from these scans, reported energies are not corrected for zero point energy contributions. These are available for selected species in the Supporting Information. Population analyses were performed with the Natural Population Analysis method.(39)

Results and Discussion

Molecular dynamics of the oxyferrous CYP19/O₂/19-oxoAD complex

A probable mechanism of Fe³⁺O₂²⁻ accumulation in CYP19 can be deduced from the X-ray crystal structure(17) of the ferric CYP19/AD complex that is in turn supported by molecular dynamics simulation of the CYP19/O₂/19-oxoAD complex. A pair of amino acids is conserved in the active site of many CYP enzymes that are critical for delivering protons to reduced oxygen intermediates. Also known as the “acid-alcohol” pair, they are typically threonine and asparatate.(40) Both experimental and theoretical studies support that protons are shuttled from the aspartate carboxyl, via the intervening threonine hydroxyl group, to the distal oxygen atom of iron-coordinated O₂.(2, 15, 41–43) Differing from this generic picture of proton delivery, the crystal structure of CYP19 illustrates a unique interaction between the bound substrate, AD, and the critical aspartate (D309). The 3-keto oxygen of AD and a carboxylate oxygen of D309 are separated by 2.7 Å, supporting a shared hydrogen bond between the two atoms.(17) Indeed, a Poisson-Boltzmann estimation(18–20) of the D309 pKa is 7.7, predicting this residue would predominantly exist in its protonated form at physiological pH and participate in a hydrogen bond.

The atomic coordinates provided by the crystal structure and the Poisson-Boltzmann calculation represent a snapshot of the Fe³⁺ CYP19/AD complex that unfortunately, best reflects the active site configuration preceding the first oxidation step. Accordingly, only limited mechanistic insight is provided for the final, deformylation step. To understand proton flow, or the abrogation thereof for stabilization of Fe³⁺O₂²⁻ prior to the final step of CYP19 catalysis, an atomistic picture of the hydrogen bond dynamics in the active site was necessary. To this end, molecular dynamics simulations of the 19-oxoAD/O₂/CYP19 complex were performed in explicit water. These trajectories also provided the initial conditions for subsequent QM/MM studies. The unique hydrogen-bond between D309 and the 3-keto oxygen atom inferred from the crystal structure is possibly present throughout the transformation of androstanedione to estrone. As our simulation evolves (50 ns total; Figure 1A), this hydrogen bond remains largely intact. In the final 20 ns when no harmonic restraints are applied between the enzyme and substrate, the mean distance between the D309 proton and the 3-keto oxygen atom is 2.00 ± 0.37 Å. This hydrogen bond indeed dominates the simulation; however, the trace of interatomic distances in Figure 1A indicates that it is transiently asunder on the nanosecond time scale. Since CYP19 also catalyzes the canonical hydroxylation reaction at the C19 methyl group of AD in the early oxidation steps, this observation is not surprising. Disruption of this hydrogen bond could permit D309 to simultaneously participate in the proton shuttle of the canonical CYP catalytic cycle.

The aldehyde of 19-oxoAD is the crucial functional group requisite for the deformylation reaction. This functional group likewise has the potential to perturb the hydrogen bond network in the vicinity of the terminal proton acceptor. However, since the Fe³⁺O₂²⁻ species accumulates with AD in the active site, perturbations abrogating proton flow from the aldehyde are likely secondary to intervention of the 3-keto oxygen atom in the “acid-alcohol” pair.(16) Nevertheless, in lieu of the hydrogen bond between the T310 hydroxyl and O₂ that would be requisite for protonation of Fe³⁺O₂²⁻, a hydrogen bond between the T310 hydroxyl and 19-oxo oxygen dominates the simulation. This is evidenced by the 2.11 ± 0.32 Å distance between these atoms over the 20 ns of unrestrained molecular dynamics simulation. Moreover, the hydrogen bond acceptor in this case is likewise transiently exchanged for the distal oxygen atom of O₂. Hence, depending on the local environment of D309, this configuration could afford the occasional protonation of reduced oxygen intermediates.

Peroxohemiacetal formation

In light of experimental observations supporting the role of $\text{Fe}^{3+}\text{O}_2^{2-}$ in the final catalytic step(5), its apparent stability in the wild-type enzyme(16), and a structure-based rationale for its accumulation(17), a careful theoretical investigation of $\text{Fe}^{3+}\text{O}_2^{2-}$ mediated aromatization was warranted. To this end, the physical admissibility of $\text{Fe}^{3+}\text{O}_2^{2-}$ initiated aromatization mechanisms were explored using QM/MM calculations. Electron paramagnetic resonance (EPR) studies of $\text{Fe}^{3+}\text{O}_2^{2-}$ P450cam support a doublet ground state for this intermediate.(44) Unless otherwise noted, we have restricted our QM/MM investigation to the doublet potential energy surface. Preliminary QM/MM geometry optimizations repeatedly failed to converge to a stable $\text{Fe}^{3+}\text{O}_2^{2-}$ species. Instead, a tetrahedral peroxohemiacetal (**PH**) species resulted from addition of distal oxygen atom to the 19-oxoAD aldehyde. This observation was confirmed in four (37.94, 39.40, 43.52, and 49.98 ns) MD snapshots near the end of the 50 ns trajectory and thus was not unique to one frame. QM/MM potential energy surfaces for the nucleophilic addition coordinate were constructed by restraining the distance between the $\text{Fe}^{3+}\text{O}_2^{2-}$ distal oxygen atom and aldehyde carbon. (Figure 2) Each surface consistently supports barrierless, exothermic (-17.6 ± 3.5 kcal/mol) addition to form the peroxohemiacetal (**PH**). The barrierless nature of this addition indicates **PH** formation would be rapid and essentially concerted with generation of $\text{Fe}^{3+}\text{O}_2^{2-}$ via reduction of the oxyferrous intermediate preceding the final step. Thus, despite the strong case built upon indirect evidence supporting an important role of $\text{Fe}^{3+}\text{O}_2^{2-}$ in the deformylation reaction, calculations support this species would elude direct experimental detection. The remainder of this Article is dedicated to describing our QM/MM investigation of $\text{Fe}^{3+}\text{O}_2^{2-}$ mediated reaction mechanisms nascent from the **PH** species in a representative MD snapshot (49.98 ns). These studies highlight alternative mechanisms invoking novel intermediates that may resign to experimental detection and characterization.

Concerted Deformylation from PH

Initial efforts were focused on identifying a concerted transition state for deformylation and 1β -hydrogen atom abstraction as originally proposed by Akhtar and coworkers.(5) We considered the reaction coordinate in which the 1β -hydrogen atom is transferred to the **PH** proximal oxygen atom with subsequent cleavage of the OO and CC bonds to produce formate, hydroxy- Fe^{3+} heme, and the readily-aromatized 1(10),4-dien-3-one steroid. The potential energy surface, illustrated in Figure S3, yields an approximate transition state corresponding 28.1 kcal/mol. This transition state leads to cleavage of the CC bond, but not the OO bond, resulting in Fe^{3+} -coordinated peroxyformic acid and the 1(10),4-dien-3-one. In light of the large energetic barrier relative to stepwise mechanisms (*vide infra*) and lack of experimental support for peroxyformic acid formation, we turned our attention to QM/MM evaluation of stepwise mechanisms initiated by cleavage of the CC or OO bonds.

Stepwise Deformylation Initiated by CC Bond Cleavage

In view of the well-characterized elimination of formate incorporating one oxygen atom from O_2 as described in the studies of Akhtar(5), we examined several mechanisms consistent with these observations. With concerted deformylation posing a high energetic barrier and the corresponding transition state leading to products not observed in experiments, we envisioned stepwise mechanisms where cleavage of the CC or OO bond could initiate deformylation.

First, illustrated in Figure 3, we describe a complete mechanism for the transformation of the **PH** intermediate to the **ES** product. From **PH**, a transition state for cleavage of the CC bond (**CC TS1**) was identified, albeit the computed barrier is 0.1 kcal/mol. Thus, this process is essentially barrierless. Single-point calculations also confirm CC cleavage barriers of < 1 kcal/mol and inclusion of the zeropoint energy correction lowers the **CC TS1** energy to 0.2

kcal/mol below that of **PH**. The weak CC bond in **PH** is attributable to hyperconjugation between the nonbonding electrons of the C19 oxyanion and the CC σ^* orbital. Accordingly, the C19-O bond contracts from 1.28 Å to 1.26 Å as it becomes more akin to a carbonyl. **CC_{TS1}** leads to the first intermediate complex (**CC_{I1}**) 18.9 kcal/mol below **PH**, which includes a Fe³⁺-peroxyformate and a closed shell 3,5(10)-dien-3-ol steroid. The latter species results from protonation of the 3-keto oxygen atom by D309 following cleavage of the CC bond. Our study of a similar deformylation/desaturation reaction catalyzed by sterol 14 α -demethylase demonstrated that the CC bond cleavage is heterolytic and resulted in a substrate-based anion intermediate.(25) This is also the case in CYP19; however, the corresponding anion is concomitantly protonated by D309. The normal mode corresponding to the single imaginary frequency in **CC_{TS1}** is dominated by the cleavage of the CC bond; hence, protonation of the 3-keto oxygen atom is a concerted albeit asynchronous event that neutralizes what would otherwise result in an intermediate anion.

Starting from **CC_{I1}**, a second transition state (**CC_{TS2}**) for cleavage of the OO bond and expulsion of formate was identified. At 14.8 kcal/mol, this barrier is regarded as the rate-limiting step in the CC-cleavage initiated mechanism. As expected, surmounting this barrier and breaking the OO bond results in formate and an iron-oxo intermediate complex (**CC_{I2}**) 32 kcal/mol below **CC_{I1}**. The barrier and exothermicities computed with the B3LYP functional are largely consistent with the PBE0 values throughout the reaction mechanism, often within 2 kcal/mol of the B3LYP results. Single-point energies for **CC_{TS2}** and **CC_{I2}** using the PBE0 functional predict a 21.2 kcal/mol barrier and 25.3 kcal/mol barrier and exothermicity, respectively. These values are 5.8 and 6.1 kcal/mol higher than those computed with the B3LYP functional and B2 basis set. It is well known that delocalization error in many density functionals results in underestimation of barriers to chemical reactions and overstabilization of delocalized radicals.(45) Recent work has suggested that the PBE0 functional may be less pathological than B3LYP in this regard.(46) Hence, the PBE0 energetics for **CC_{TS2}** and **CC_{I2}** may be more reliable. Nevertheless, consistent conclusions are drawn from both levels of theory.

The most interesting and surprising characteristic of the OO-cleavage step is that the deformylated substrate is not a spectator. OO cleavage is coupled to electron and proton transfer processes, the physical bases of which are best understood by considering differences in the spin density distributions in the QM regions of **CC_{I1}**, **CC_{TS2}**, and **CC_{I2}** illustrated in Figure 4A. Like **CC_{I1}**, the 3,5(10)-dien-3-ol of **CC_{TS2}** is neutral and lacks appreciable spin density. Concomitantly, the spin density localized to the incipient formate shifts from zero in **CC_{I1}** to -0.34 in **CC_{TS2}**. This accumulation of an unpaired electron on formate suggests the OO bond is breaking homolytically, and would therefore be expected to afford the formyl radical and an iron-oxo species. However, this is not the case as illustrated by the spin density distribution of **CC_{I2}**, which unequivocally assigns the formyl species as the formate anion ($\rho^{\text{HCOO}} = -0.01$, $q^{\text{HCOO}} = -0.98$). Albeit, the iron-oxo intermediate produced is the one-electron reduced form of Cpd I, known as Compound II (Cpd II) that is expected from homolytic OO cleavage. Population analyses confirm this species as Cpd II, which maintains a triplet electronic configuration on the Fe⁴⁺O²⁻ unit ($\rho^{\text{FeO}} = 2.05$), and a closed-shell porphyrin ($\rho^{\text{Porphyrin}} = -0.04$). It appears that during the transformation of **CC_{TS2}** to **CC_{I2}**, the formyl radical undergoes single-electron reduction to formate, which is illustrated by accumulation of antiparallel spin density localized to the 3,5(10)-dien-3-ol substrate. The electron transfer is coupled to deprotonation of the 3-keto oxygen atom by D309, resulting in a neutral 3,5(10)-dien-3-oxyl radical intermediate. The spin density localized to the 3,5(10)-dien-3-oxyl radical is antiparallel to that of the Fe⁴⁺O²⁻ unit, consistent with an overall doublet electronic configuration. The combined redistribution of spin density, charge, and protonation state associated with cleavage of the

OO bond are consistent with a proton-coupled electron transfer mechanism which circumvents the accumulation of a radical cation intermediate.

In the CC cleavage initiated reaction, a proton has been cyclically relayed between D309 and the 3-keto oxygen avoiding accumulation of charge on the deformylated substrate. In our recent study of a similar mechanism in sterol 14 α -demethylase catalysis, OO scission is likewise coupled to electron transfer from a steroid anion to the incipient formate. However, unlike CYP19 the acidic residue in the “acid-alcohol pair” is replaced with a histidinium, that does not seem to establish any direct interaction with the substrate.(25) To further illustrate the nature of the CC cleavage in CYP19 and potentially quantitate the energetic stabilization of **CC11**, **CCTS2**, and **CC12** imparted by the cyclical proton transfer, the potential energy surfaces for OO cleavage were mapped while the proton was restrained either to D309 or the 3,5(10)-dien-3-ol. Both restrained and unrestrained potential energy surfaces are superimposed in Figure 4B. When the proton is restrained to D309 (Figure 4B, blue curve), and not transferred to the 3-keto oxygen, indeed a 3,5(10)-dien-3-olate anion ($q = -0.85$) is formed at large values of the OO distance. Restraint of the proton to D309 in **CC11** destabilizes the coordinate by 6.8 kcal/mol. Doing so does not appreciably change the barrier for cleavage of the OO bond; however, the transition state does occur somewhat earlier. Conversely, when the proton is restrained to the 3-keto oxygen (Figure 4B, red curve), the restrained and unrestrained potential energy surfaces are essentially identical up to the point corresponding to **CCTS2**, which then diverge until the surface is maximally destabilized by 8.0 kcal/mol relative to **CC12**. This destabilization is attributable to the cationic nature ($q = +0.74$) of the radical species resulting from failure to relinquish the proton to D309. Taken together, these results indicate that the cyclical proton transfer does not necessarily impart a kinetic advantage by stabilizing the OO cleavage transition state. Rather, this phenomenon complements the thermodynamic driving force to form **CC11** and **CC12** by sidestepping the formation of charged catalytic intermediates.

Isotope studies also indicate both 1 β - and 2 β -hydrogens are removed from AD during the final catalytic step.(6, 8, 10, 11) The 1 β - and 2 β -hydrogen atoms are 2.4 and 2.8 Å from the Cpd II oxygen atom in **CC12**, respectively. Due to the proximity of the 1 β -hydrogen for abstraction, the potential energy surface for transfer of this atom to Cpd II was mapped and is illustrated in Supporting Figure S4. The approximate transition state (**CCTS3**) reveals a barrier of 13.4 kcal/mol. Hydrogen atom transfer in this step is confirmed by loss of the -0.99 spin density associated with the 3,5(10)-dien-3-oxy radical in **CC12** to zero in the 1(10),4-dien-3-one of **CC13**. Given the triradicaloid nature of **CC12** (triplet electronic configuration on FeO with an antiparallel electron localized to the steroid A ring), spin inversion of the substrate-localized electron will likely result in a degenerate quartet state due to weak coupling of this electron to the Fe⁴⁺O²⁻ triplet pair. Indeed, the **CC12** quartet and doublet are essentially degenerate, with an energetic spacing of 0.04 kcal/mol. The barrier for 1 β -hydrogen abstraction on the quartet surface is 13.5 kcal/mol, nearly indistinguishable from the barrier computed on the doublet surface. Both the doublet and quartet states of the **CC13** complex include a hydroxide-coordinated Fe³⁺ heme complex; however the energetic degeneracy is broken with the doublet state favored by 5.1 kcal/mol. In the doublet, the oxidation state of Fe³⁺ is confirmed by the d⁵ electronic configuration and atomic spin density of 0.97.

The role of the enzyme active site and the timing of the stereoselective loss of the 2 β -hydrogen in the third catalytic step have been the subject of debate and investigated by several groups. Brodie and Fishman initially demonstrated that CYP19 specifically removes the 2 β -hydrogen from AD.(8, 9) Following the synthesis of [2 β -²H]-19-oxoandrostenedione, Cole and Robinson confirmed that the 2 β -hydrogen is stereoselectively removed in the final step.(11) In these experiments, epimerization of C2 or exchange of the 2 β -²H label with

solvent did not occur in the presence of enzyme without NADPH, suggesting the requisite base for enolization is not generated in the active site until after heme reduction. Furthermore, neither the crystal structure(17) or the MD simulations described herein illuminate a putative base capable of mediating stereoselective enolization. A possible explanation for these experimental observations is illustrated by **CC_I3**, where the hydroxy-Fe³⁺ oxygen is 2.5 Å from the 1(10),4-dien-3-one 2β-hydrogen and D309 is hydrogen-bonded to the 3-keto oxygen. From this configuration, a transition state (**CC_{TS}4**) for stereospecific enolization with a barrier of 10.9 kcal/mol was identified and as expected, connects **CC_I3** to the aromatized product complex (**CC_{ES}**) including estrone and H₂O-Fe³⁺ heme. As expected, the -22.8 kcal/mol exothermicity for this step is attributable to the construction of the estrone aromatic ring. Subsequent single-point calculations confirm the energetics obtained at the optimization level of theory supporting facile, enzyme-mediated enolization. Calculations using the B2 basis set indicate the computed values are insensitive to the increase in basis set flexibility, with the barrier and exothermicities varying only 0.1 and -1.6 kcal/mol, respectively from B3LYP/B1. Single-point calculations at the PBE0/B2 level of theory predict a slightly smaller, 8.6 kcal/mol barrier and somewhat greater, -27.3 kcal/mol, exothermicity. In combination with these energetics, the proximity of the hydroxy-Fe³⁺ heme and capacity of D309 to protonate the 3-keto oxygen atom offers a convenient explanation for the stereoselective loss of the 2β-hydrogen in the final step and its dependency on NADPH. The apparent optimal alignment of atoms undergoing changes in bonding during enolization permits speculation about the mechanistic origins of other observations made by Cole and Robinson.(11) These investigators also synthesized and similarly evaluated the stereoselectivity of 2β-hydrogen loss from [2β-²H]-19-oxotestosterone. Unexpectedly, the 2β-hydrogen was not stereoselectively removed. This result was attributed to the possibility that the 19-oxotestosterone 17β-hydroxyl perturbs the binding mode relative to that of 19-oxoandrostenedione such that it is ineffectively positioned for 2β-deprotonation by a then unidentified active site base. Assuming hydroxy-Fe³⁺ is the critical base, it is reasonable to speculate that the 1(10),4-dien-3-one intermediate derived from 19-oxotestosterone may indeed be ineffectively aligned for 2β-deprotonation and is instead prematurely released from the enzyme to undergo aromatization nonstereoselectively in the aqueous environment.

Stepwise Deformylation Initiated by OO Bond Cleavage

Second, we considered a stepwise mechanism initiated by cleavage of the OO bond in **PH**. The intermediates and transition states of which are illustrated in Figure 5. In contrast to the essentially barrierless CC cleavage in **PH** illustrated in Figure 3, the transition state for OO cleavage is attained with a substantially higher, 10.6 kcal/mol barrier at the B3LYP/B1 level of theory. A marginally higher 11.5 kcal/mol barrier is predicted with increasing the basis set flexibility to B3LYP/B2. This barrier increases further to 14.9 kcal/mol with the PBE0 density functional and the B2 basis set. Subsequent formation of the intermediate (**OO_I11**) is 4.4 kcal/mol endothermic at the optimization level of theory (B1), which is also affirmed by single-point calculations with the B2 basis set and the PBE0 density functional. The resulting intermediate, **OO_I11**, is composed of Cpd II ($\rho_{\text{FeO}} = 2.03$; $\rho_{\text{Porphyrin}} = -0.04$) as well as a dioxyradical anion ($\rho_{\text{Substrate}} = -0.98$). The composition of this latter species illustrates that cleavage of the OO and CC bond are not concerted. Nevertheless, as in the stepwise CC cleavage pathway, the Cpd II oxygen atom is likewise 2.3 Å from the 1β-hydrogen atom. However, failure of the oxyanion to leave as formate thereby sterically and electrostatically obstructs Cpd II's access to the 1β-hydrogen atom, accordingly increasing the barrier corresponding to **OO_{TS}2** to a value 6.8 kcal/mol higher (20.2 versus 13.4 kcal/mol) than that computed in the analogous transition state where formate has already been expelled (**CC_{TS}3**). Indeed, abstraction of the 1β-hydrogen atom and cleavage of the CC bond in **OO_I11** are concerted, leading to the hydroxy-Fe³⁺ and a 1(10),4-dien-3-one. As in **CC_I3**, hydroxide

is likewise positioned to deprotonate the 2β -hydrogen and generate the final product complex including estrone, aquaferrous CYP19, and formate. This transition state has a barrier 9.9 kcal/mol, similar to the 10.9 kcal/mol barrier computed for the same reaction in the CC pathway. Notably, the D309 proton is never relayed to the 3-keto oxygen atom in the OO cleavage initiated pathway until the stereoselective enolization occurs. In summary, the initial cleavage of the OO bond proceeds with a substantially higher barrier and is endothermic, hence it is uncompetitive with the kinetic and thermodynamic advantage held by the CC cleavage pathway.

Deformylation from the protonated PH

The molecular dynamics simulations do not entirely exclude a hydrogen-bonding configuration required to shuttle protons to T310. (Figure 1) The T310 hydrogen bond is largely diverted from the distal oxygen atom of O_2 to the C19 aldehyde of 19-oxoAD. This aldehyde is not sufficiently basic to act as proton acceptor in the oxyferrous enzyme; however following reduction and barrierless addition of the distal oxygen atom of the $Fe^{3+}O_2^{2-}$ species, this atom resembles an alkoxy anion, where the atomic charge on the aldehyde oxygen is -0.92. (Figure 3) We envisioned the possibility that the proton shuttle is diverted from the distal oxygen atom such that the **PH** becomes the terminal proton acceptor. Intermediates and transition states for the deformylation mechanism nascent from the protonated **PH**, **HPH** are illustrated in Figure 6. Protonation of the oxyanion abrogates the hyperconjugation attributed to the **PH** oxyanion that reduced the barrier for cleavage of this bond. The barrier for CC cleavage in the **HPH** is prohibitively high, greater than 39 kcal/mol. Hence, this pathway was not considered further. In contrast to the unprotonated case, the preferred path from **HPH** is OO cleavage via the transition state **OOHTS1** with a 12.7 kcal/mol barrier. Like the unprotonated case, OO cleavage is likewise endothermic by 6.7 kcal/mol, with the subsequent intermediate **OOHI1** including Cpd II optimally configured for 1β -hydrogen abstraction. In this pathway, the protonated oxyradical moiety also obstructs access to the 1β position elevating the barrier of **OOHTS2** by 4.0 kcal/mol relative to that corresponding to **CCTS3**. 1β -hydrogen atom abstraction and dissociation of formic acid are concerted; however, formic acid is subsequently deprotonated by the hydroxy- Fe^{3+} species resulting in aquaferrous CYP19, formate, and the 1(10),4-dien-one represented by **OOHI2**. Unlike the deprotonated pathways, direct protonation of hydroxy- Fe^{3+} abolishes the active site base that is positioned for stereospecific deprotonation of the 2β position. The 1(10),4-dien-3-one would indeed be readily converted to the aromatic product upon dissociation from the enzyme into the aqueous environment, although no stereoselectivity would be observed. We acknowledge that in the configuration we have selected for QM/MM study the formic acid is positioned to protonate the hydroxyferric intermediate. Nevertheless, it is reasonable to propose that in other configurations formic acid is expelled from the enzyme or deprotonated by an alternative base in the protein environment. If this occurs, the mechanism leading from **HPH** would likewise converge to the stereospecific enolization step involving the 2β - and D309 protons.

Conclusions

Over the past five decades, experimental data has accumulated indirectly implicating the $Fe^{3+}O_2^{2-}$ species in the final step of the CYP19 reaction. However, arguments arising from interpretation of this data have met resistance since $Fe^{3+}O_2^{2-}$ has eluded direct characterization in wild-type P450cam.(15) The recent demonstration that the $Fe^{3+}O_2^{2-}$ species does indeed accumulate in CYP19 has garnered new interest in $Fe^{3+}O_2^{2-}$ as a key intermediate in the enigmatic aromatization mechanism. With the recent solution high-resolution crystal structure of human CYP19,(17) we successfully investigated the hydrogen-bond dynamics and evaluated plausible mechanisms for $Fe^{3+}O_2^{2-}$ mediated

aromatization. Molecular dynamics simulation of the oxyferrous CYP19/19-oxoAD complex revealed that D309 in the conserved “acid-alcohol” pair is likely protonated at physiological pH and forms a stable hydrogen bond to the 3-keto oxygen atom of AD. This hydrogen bond apparently serves as gate in the proton shuttle, hindering proton flow thereby affording accumulation of the $\text{Fe}^{3+}\text{O}_2^{2-}$ species. Our simulations also illustrate that the 19-aldehyde diverts the T310 hydrogen bond from the distal O_2 atom. This would likewise be expected to delay proton delivery; however, since $\text{Fe}^{3+}\text{O}_2^{2-}$ accumulation is observed with AD present in the active site, we speculate that the dominant feature affording observation of $\text{Fe}^{3+}\text{O}_2^{2-}$ is hydrogen bonding between D309 and the substrate.

Multiple mechanisms for $\text{Fe}^{3+}\text{O}_2^{2-}$ mediated deformylation were considered but the stepwise mechanism illustrated in Scheme 2 involving initial cleavage of the CC bond in **PH** demonstrated a clear kinetic advantage over others. These calculations support that upon reduction of the oxyferrous species to $\text{Fe}^{3+}\text{O}_2^{2-}$, generation of **PH** and CC-bond cleavage would occur in a single concerted step. (Scheme 2, **A** → **B**) Thus, we predict $\text{Fe}^{3+}\text{O}_2^{2-}$ would circumvent experimental observation and characterization or at the least, present extreme difficulties. The first heme-oxygen intermediate to be observed would be the Fe^{3+} peroxyformate (**B**). This species subsequently extrudes formate in a manner consistent with isotope experiments supporting incorporation of one atom from O_2 into formate.(5) (**B** → **C**) Concomitant generation of Compound II mediates the 1 β -hydrogen atom abstraction (**C** → **D**), which is followed by a stereoselective enolization reaction that removes the 2 β -hydrogen with hydroxy- Fe^{3+} serving as the base (**D** → **E**). The stereoselective enolization requires optimal alignment of hydroxy- Fe^{3+} , the substrate, and D309. The requisite alignment of these functional groups may explain why unlike androstenedione, CYP19-catalyzed testosterone aromatization does not result in stereoselective removal of the 2 β -hydrogen. The 17 β -hydroxyl of testosterone may sufficiently perturb its orientation relative to the heme such that the preceding 1(10),4-dien-3-one undergoes aromatization following premature dissociation from the enzyme.

Supplementary Material

Refer to Web version on PubMed Central for supplementary material.

Acknowledgments

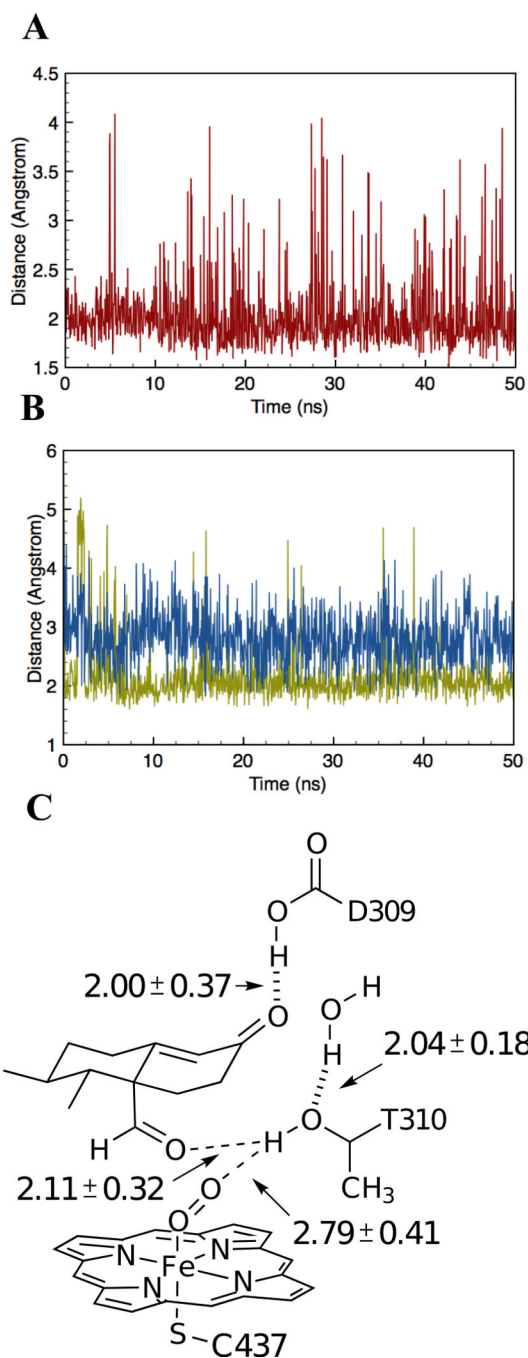
Computational resources were provided by the Ohio Supercomputer Center and the Max Planck Institute for Kohlenforschung.

References

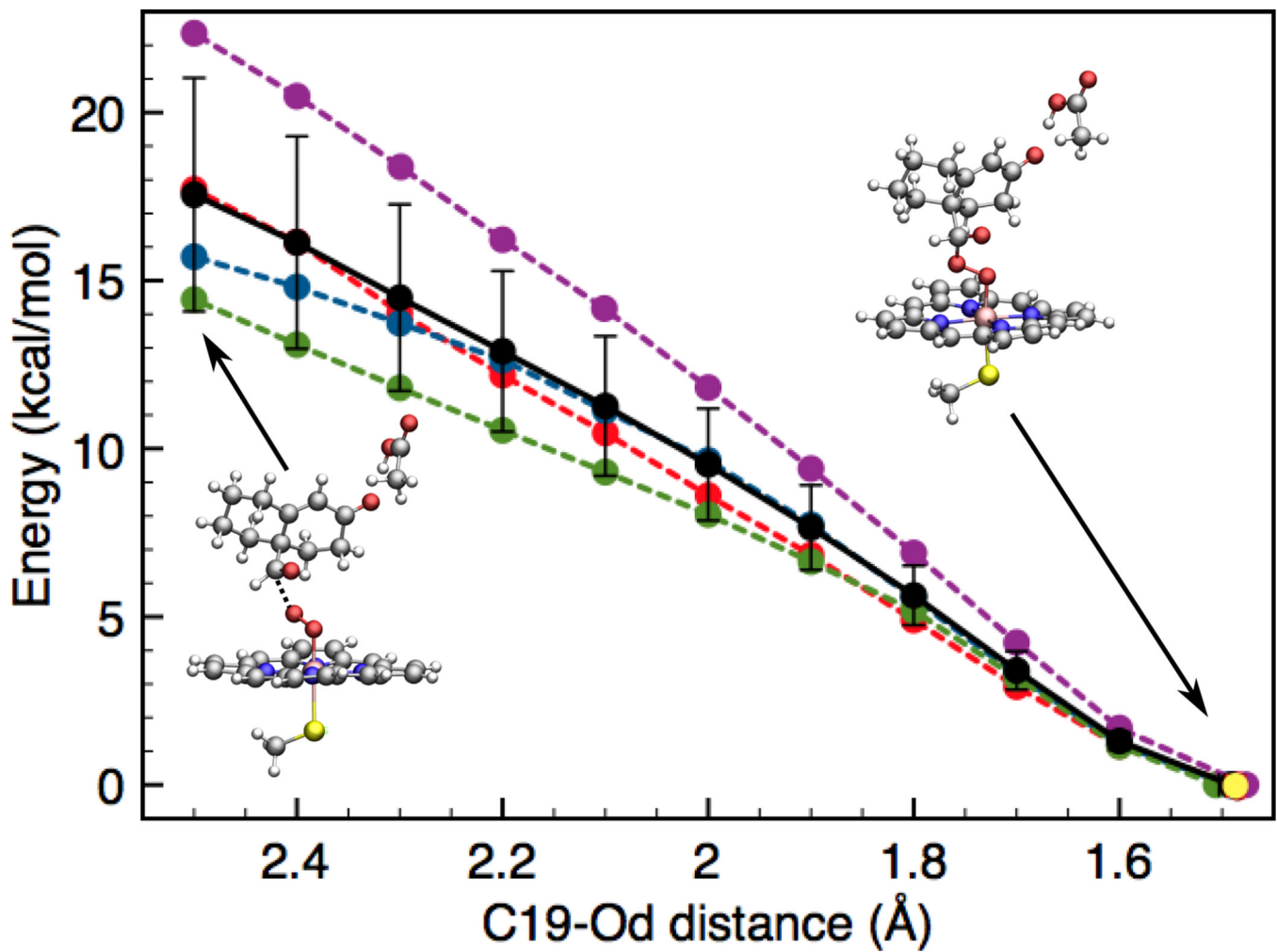
1. Ortiz de Montellano, PR. Cytochrome P450: structure, mechanism, and biochemistry. Vol. Vol. 3. New York: Kluwer Academic/Plenum Publishers; 2005.
2. Shaik S, Cohen S, Wang Y, Chen H, Kumar D, Thiel W. P450 enzymes: their structure, reactivity, and selectivity-modeled by QM/MM calculations. Chem. Rev. 2010; 110:949–1017. [PubMed: 19813749]
3. Brueggemeier RW, Hackett JC, Diaz-Cruz ES. Aromatase inhibitors in the treatment of breast cancer. Endocrine Rev. 2005; 26:331–345. [PubMed: 15814851]
4. Sohl CD, Guengerich FP. Kinetic analysis of the three-step steroid aromatase reaction of human cytochrome P450 19A1. J. Biol. Chem. 2010; 285:17734–17743. [PubMed: 20385561]
5. Akhtar M, Calder MR, Corina DL, Wright JN. Mechanistic studies on C-19 demethylation in oestrogen biosynthesis. Biochem. J. 1982; 201:569–580. [PubMed: 7092812]
6. Morato T, Raab K, Brodie HJ, Hayano M, Dorfman RI. The Mechanism of Estrogen Biosynthesis. J. Am. Chem. Soc. 1962; 84:3764–3766.

7. Townsley JD, Brodie HJ. Mechanism of estrogen biosynthesis. III. Stereochemistry of aromatization of C19 and C18 steroids. *Biochemistry*. 1968; 7:33–40. [PubMed: 4394749]
8. Brodie HJ, Kripalani KJ, Possanza G. Mechanism of estrogen biosynthesis. VI. The stereochemistry of hydrogen elimination at C-2 during aromatization. *J. Am. Chem. Soc.* 1969; 91:1241–1242. [PubMed: 5780508]
9. Fishman J, Guzik H. Stereochemistry of estrogen biosynthesis. *J. Am. Chem. Soc.* 1969; 91:2805–2806. [PubMed: 5784955]
10. Fishman J, Guzik H, Dixon D. Stereochemistry of estrogen biosynthesis. *Biochemistry*. 1969; 8:4304–4309. [PubMed: 5353101]
11. Cole PA, Robinson CH. Conversion of 19-oxo[2 beta-2H]androgens into oestrogens by human placental aromatase. An unexpected stereochemical outcome. *Biochem. J.* 1990; 268:553–561. [PubMed: 2363692]
12. Wertz DL, Sisemore MF, Selke M, Driscoll J, Valentine JS. Mimicking cytochrome P-450 2B4 and aromatase: Aromatization of a substrate analogue by a peroxy Fe(III) porphyrin complex. *J. Am. Chem. Soc.* 1998; 120:5331–5332.
13. Annaraj J, Suh Y, Seo MS, Kim SO, Nam W. Mononuclear nonheme ferric-peroxy complex in aldehyde deformylation. *Chem. Comm.* 2005; 36:4529–4531. [PubMed: 16158103]
14. Park MJ, Lee J, Suh Y, Kim J, Nam W. Reactivities of mononuclear non-heme iron intermediates including evidence that iron(III)-hydroperoxy species is a sluggish oxidant. *J. Am. Chem. Soc.* 2006; 128:2630–2634. [PubMed: 16492048]
15. Davydov R, Makris TM, Kofman V, Werst DE, Sligar SG, Hoffman BM. Hydroxylation of camphor by reduced oxy-cytochrome P450cam: mechanistic implications of EPR and ENDOR studies of catalytic intermediates in native and mutant enzymes. *J. Am. Chem. Soc.* 2001; 123:1403–1415. [PubMed: 11456714]
16. Gant SL, Denisov IG, Grinkova YV, Sligar SG. The critical iron-oxygen intermediate in human aromatase. *Biochem. Biophys. Res. Comm.* 2009; 387:169–173. [PubMed: 19591804]
17. Ghosh D, Griswold J, Erman M, Pangborn W. Structural basis for androgen specificity and oestrogen synthesis in human aromatase. *Nature*. 2009; 457:219–223. [PubMed: 19129847]
18. Bas DC, Rogers DM, Jensen JH. Very fast prediction and rationalization of pK(a) values for protein-ligand complexes. *Proteins*. 2008; 73:765–783. [PubMed: 18498103]
19. Dolinsky TJ, Czodrowski P, Li H, Nielsen JE, Jensen JH, Klebe G, Baker NA. PDB2PQR: expanding and upgrading automated preparation of biomolecular structures for molecular simulations. *Nucleic Acids Res.* 2007; 35:W522–W525. [PubMed: 17488841]
20. Kieseritzky G, Knapp EW. Improved pK(a) prediction: Combining empirical and semimicroscopic methods. *J. Comput. Chem.* 2008; 29:2575–2581. [PubMed: 18470967]
21. MacKerell AD, Bashford D, Bellott M, Dunbrack RL, Evanseck JD, Field MJ, Fischer S, Gao J, Guo H, Ha S, Joseph-McCarthy D, Kuchnir L, Kuczera K, Lau FTK, Mattos C, Michnick S, Ngo T, Nguyen DT, Prodhom B, Reiher WE, Roux B, Schlenkrich M, Smith JC, Stote R, Straub J, Watanabe M, Wiorkiewicz-Kuczera J, Yin D, Karplus M. All-Atom Empirical Potential for Molecular Modeling and Dynamics Studies of Proteins. *J. Phys. Chem. B.* 1998; 102:3586–3616.
22. Bathelt CM, Zurek J, Mulholland AJ, Harvey JN. Electronic structure of compound I in human isoforms of cytochrome P450 from QM/MM modeling. *J. Am. Chem. Soc.* 2005; 127:12900–12908. [PubMed: 16159284]
23. Oda A, Yamaotsu N, Hirono S. New AMBER force field parameters of heme iron for cytochrome P450s determined by quantum chemical calculations of simplified models. *J. Comput. Chem.* 2005; 26:818–826. [PubMed: 15812779]
24. Cournia Z, Smith JC, Ullmann GM. A molecular mechanics force field for biologically important sterols. *J. Comput. Chem.* 2005; 26:1383–1399. [PubMed: 16028234]
25. Sen K, Hackett JC. Peroxo-iron mediated deformylation in sterol 14alpha-demethylase catalysis. *J. Am. Chem. Soc.* 2010; 132:10293–10305. [PubMed: 20662512]
26. Vaiana AC, Cournia Z, Costescu IB, Smith JC. AFMM: A molecular mechanics force field vibrational parametrization program. *Comp. Phys. Commun.* 2005; 167:34–42.

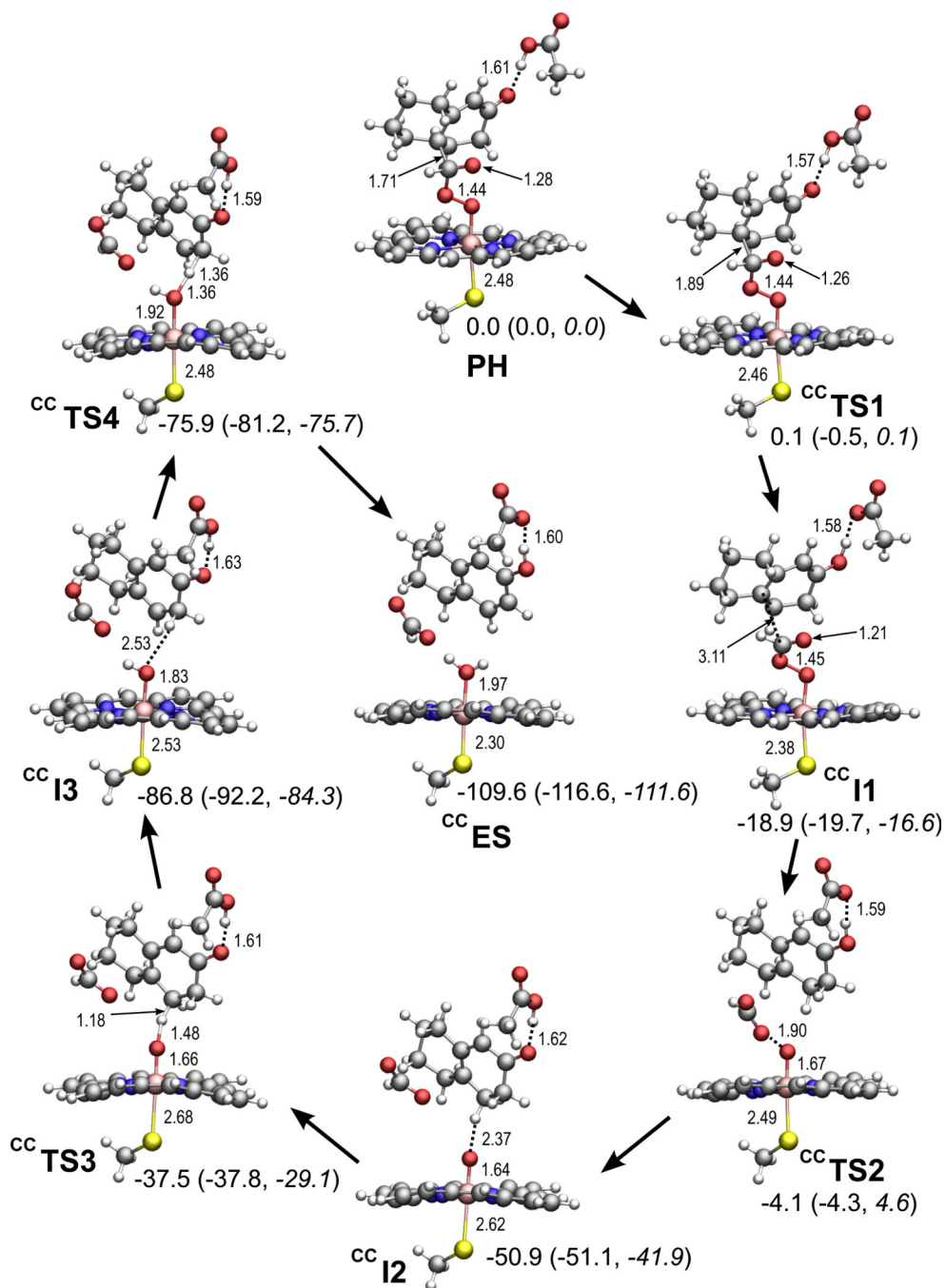
- NIH-PA Author Manuscript NIH-PA Author Manuscript NIH-PA Author Manuscript
27. Breneman, Wiberg. Determining Atom-Centered Monopoles from Molecular Electrostatic Potentials - The Need for High Sampling Density in Formamide Conformational Analysis. *J. Comput. Chem.* 1990; 11:361.
 28. Phillips JC, Braun R, Wang W, Gumbart J, Tajkhorshid E, Villa E, Chipot C, Skeel RD, Kale L, Schulten K. Scalable molecular dynamics with NAMD. *J. Comput. Chem.* 2005; 26:1781–1802. [PubMed: 16222654]
 29. Sherwood P, de Vries AH, Guest MF, Schreckenbach G, Catlow CRA, French SA, Sokol AA, Bromley ST, Thiel W, Turner AJ, Billeter S, Terstegen F, Thiel S, Kendrick J, Rogers SC, Casci J, Watson M, King F, Karlsen E, Sjøvoll M, Fahmi A, Schafer A, Lennartz C. QUASI: A general purpose implementation of the QM/MM approach and its application to problems in catalysis. *J. Mol. Struct.: THEOCHEM.* 2003; 632:1–28.
 30. Ahlrichs R, Bär M, Häser M, Horn H, Kölmel C. Electronic structure calculations on workstation computers: The program system turbomole. *Chem. Phys. Lett.* 1989; 162:165–169.
 31. Smith W, Forester TR. DL_POLY_2.0: a general-purpose parallel molecular dynamics simulation package. *J. Mol. Graph.* 1996; 14:136–141. [PubMed: 8901641]
 32. Bakowies D, Thiel W. Hybrid Models for Combined Quantum Mechanical and Molecular Mechanical Approaches. *J. Phys. Chem.* 1996; 100:10580–10594.
 33. Lee C, Yang W, Parr RG. Development of the Colle-Salvetti correlation-energy formula into a functional of the electron density. *Phys. Rev. B.* 1988; 37:785–789.
 34. Becke AD. Density-functional exchange-energy approximation with correct asymptotic behavior. *Phys. Rev. A.* 1988; 38:3098–3100. [PubMed: 9900728]
 35. Perdew JP. Density-functional approximation for the correlation energy of the inhomogeneous electron gas. *Phys. Rev. B.* 1986; 33:8822–8824.
 36. Perdew JP, Burke K, Ernzerhof M. Generalized Gradient Approximation Made Simple. *Phys. Rev. Lett.* 1996; 77:3865–3868. [PubMed: 10062328]
 37. Perdew JP, Ernzerhof M, Burke K. Rationale for mixing exact exchange with density functional approximations. *J. Chem. Phys.* 1996; 105:9982–9985.
 38. Wachters AJH. Gaussian Basis Set for Molecular Wavefunctions Containing Third-Row Atoms. *J. Chem. Phys.* 1970; 52:1033–1036.
 39. Reed AE, Weinstock RB, Weinhold F. Natural population analysis. *J. Chem. Phys.* 1985; 83:735–746.
 40. Nebert DW, Nelson DR, Coon MJ, Estabrook RW, Feyereisen R, Fujii-Kuriyama Y, Gonzalez FJ, Guengerich FP, Gunsalus IC, Johnson EF. The P450 superfamily: update on new sequences, gene mapping, and recommended nomenclature. *DNA Cell Biol.* 1991; 10:1–14. [PubMed: 1991046]
 41. Denisov IG, Makris TM, Sligar SG, Schlichting I. Structure and chemistry of cytochrome P450. *Chem. Rev.* 2005; 105:2253–2277. [PubMed: 15941214]
 42. Schlichting I, Berendzen J, Chu K, Stock AM, Maves SA, Benson DE, Sweet RM, Ringe D, Petsko GA, Sligar SG. The catalytic pathway of cytochrome p450cam at atomic resolution. *Science.* 2000; 287:1615–1622. [PubMed: 10698731]
 43. Shaik S, Kumar D, de Visser SP, Altun A, Thiel W. Theoretical perspective on the structure and mechanism of cytochrome P450 enzymes. *Chem. Rev.* 2005; 105:2279–2328. [PubMed: 15941215]
 44. Davydov R, Kappl R, Hütermann J, Peterson JA. EPR-spectroscopy of reduced oxyferrous-P450cam. *FEBS Lett.* 1991; 295:113–115. [PubMed: 1662641]
 45. Cohen AJ, Mori-Sanchez P, Yang W. Insights into current limitations of density functional theory. *Science.* 2008; 321:792–794. [PubMed: 18687952]
 46. Johnson ER, Mori-Sanchez P, Cohen AJ, Yang W. Delocalization errors in density functionals and implications for main-group thermochemistry. *J. Chem. Phys.* 2008; 129:204112.

**Figure 1.**

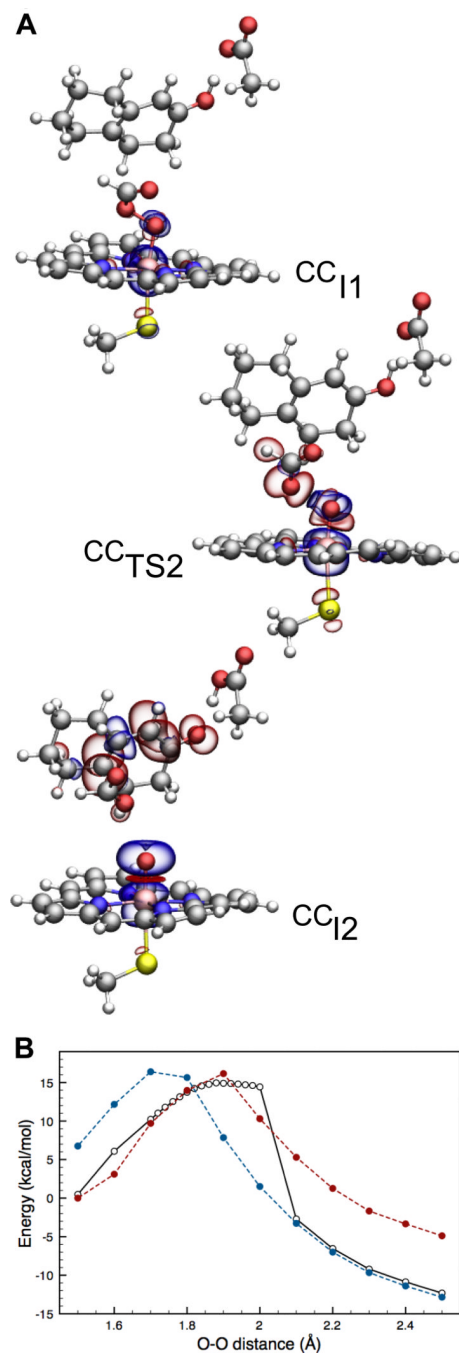
A) Distance between the D309 proton and the 3-keto oxygen atom over 50 ns of NPT MD simulation. B) Distances between the T310 proton and the 19-oxo oxygen (green) and the distal oxygen atom (blue). C) Average hydrogen bond distances \pm S. D. over the final 20 ns of the 50 ns simulation.

**Figure 2.**

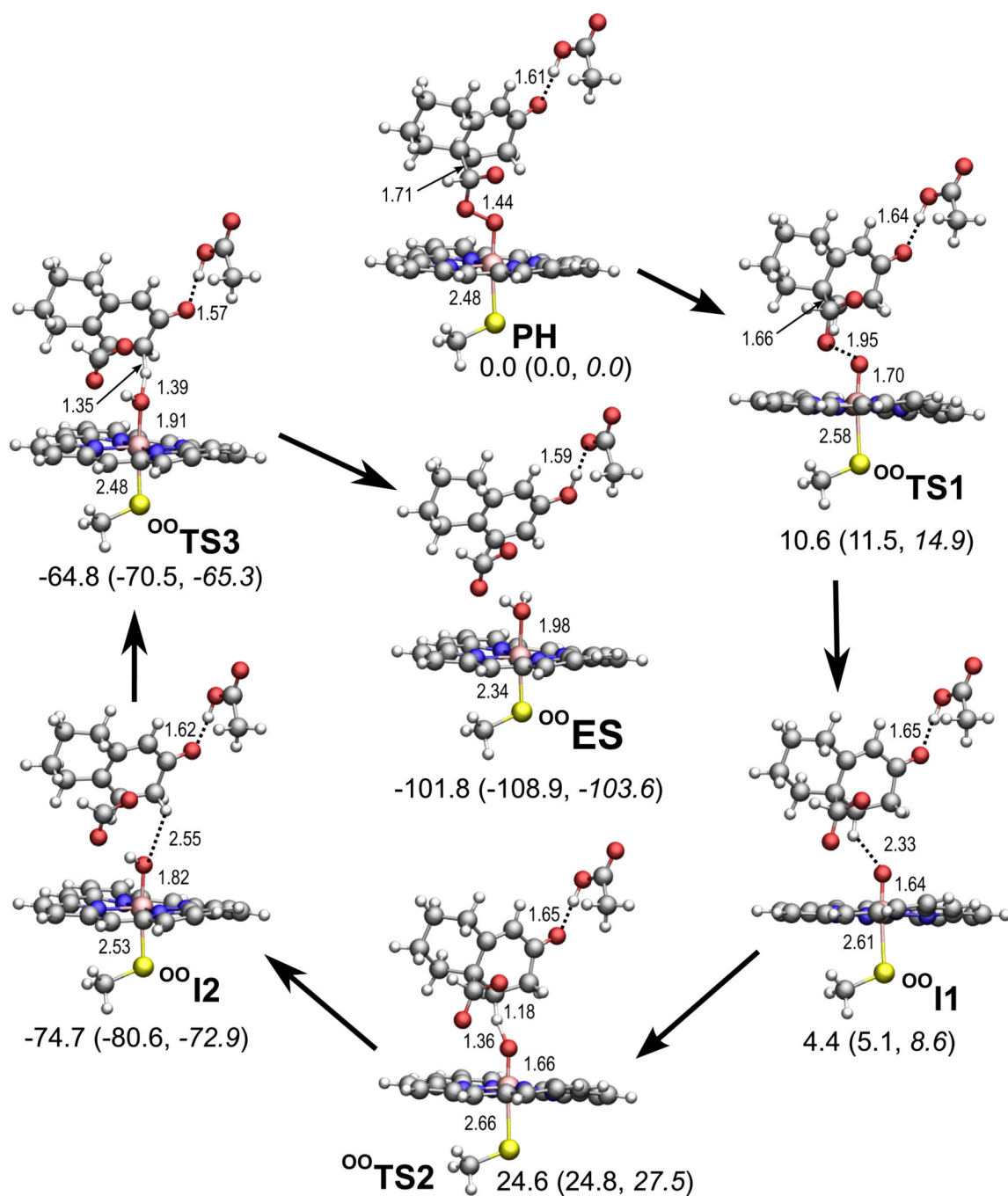
B3LYP/B1:CHARMM22 potential energy surfaces for addition of the peroxy distal oxygen atom to 19-oxoAD. Potential energy surfaces were constructed from snapshots corresponding to 37.94 (green), 39.40 (purple), 43.52 (blue), and 49.98 (red) ns of the MD simulation. The mean potential energy \pm standard deviation is illustrated black. The yellow point corresponds to the fully-optimized geometry of the peroxohemiacetal species derived from the 49.98 ns trajectory point.

**Figure 3.**

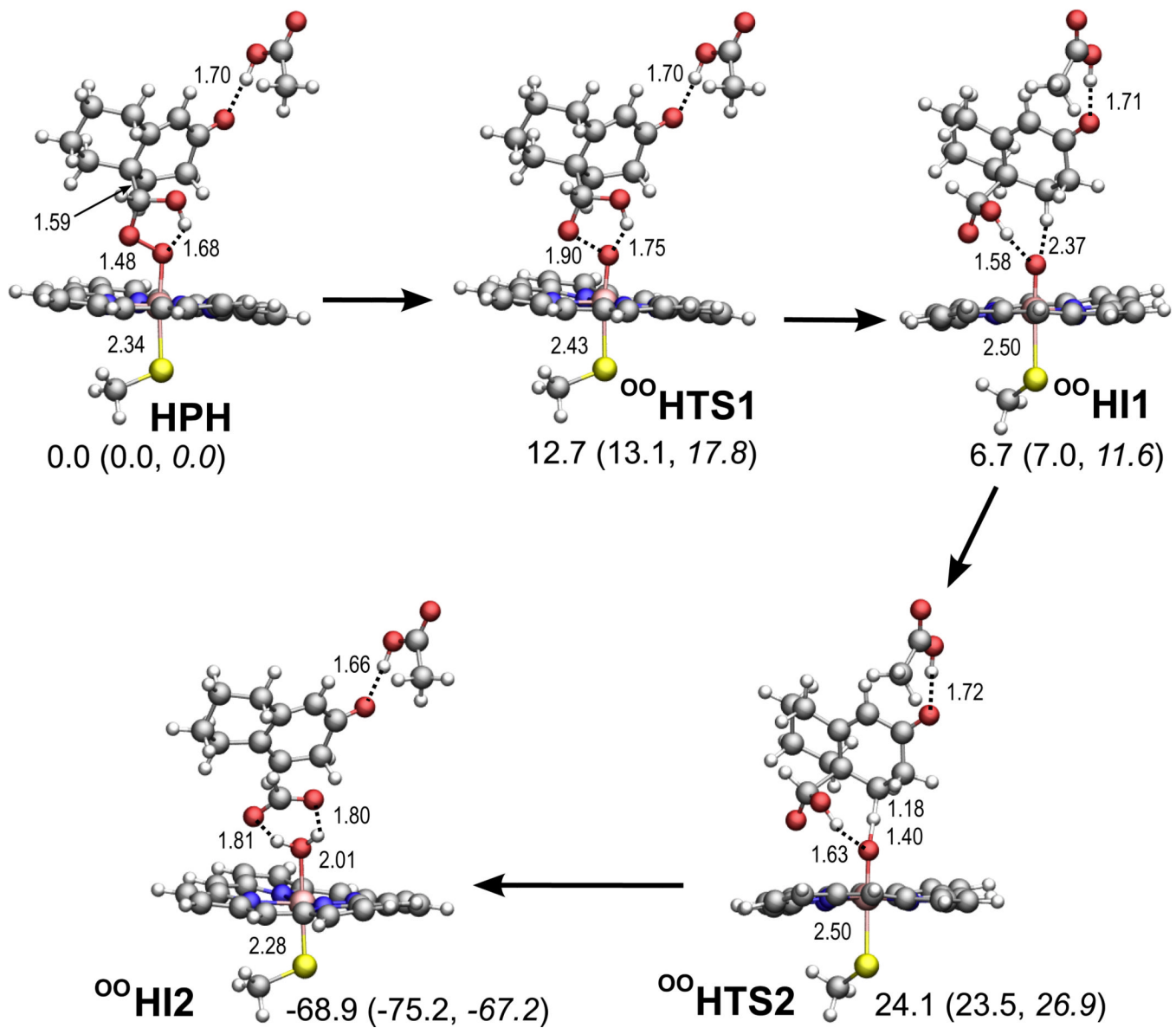
Relative B3LYP/B1:CHARMM22 energetics and structures of intermediates and transition states in the stepwise, CC-cleavage initiated aromatization pathway nascent from the peroxyhemiacetal. Single-point energies at the B3LYP/B2:CHARMM22 and PBE0/B2:CHARMM22 levels of theory are represented in parentheses and italics, respectively. Energies and distances are reported in kcal/mol and Angstroms.

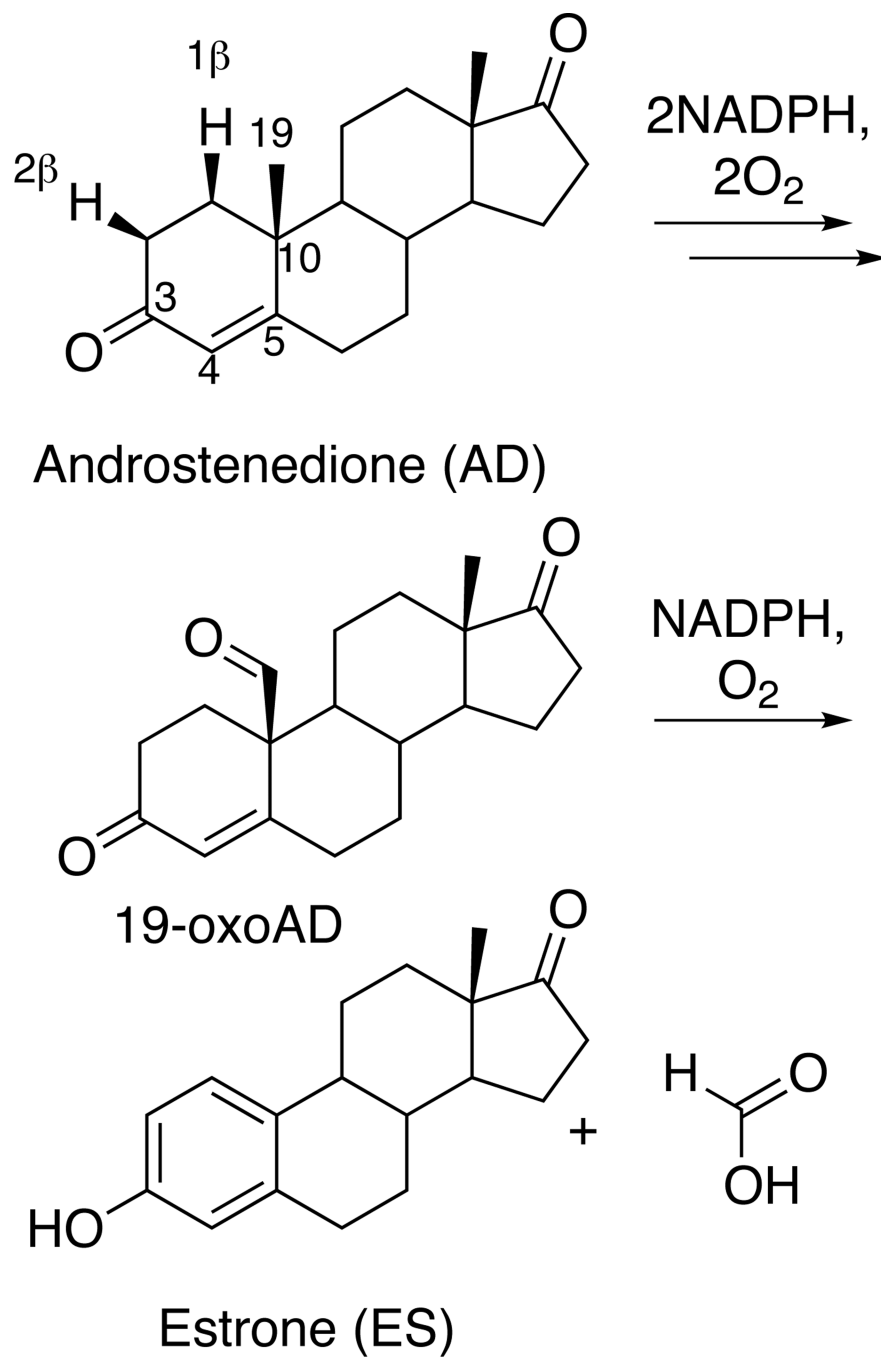
**Figure 4.**

A) Spin difference density isocontours for CC-cleavage reaction intermediates. Accumulation of α - and β - spin density are represented with blue and red surfaces plotted with an isocontour value of 0.002 a.u., respectively. B) B3LYP/B1:CHARMM22 potential energy surfaces for O-O cleavage in CC_{I1} with the proton restrained to either the 19-oxoAD 3-keto group (red) or D309 (blue). The surface with the unrestrained proton is illustrated in black.

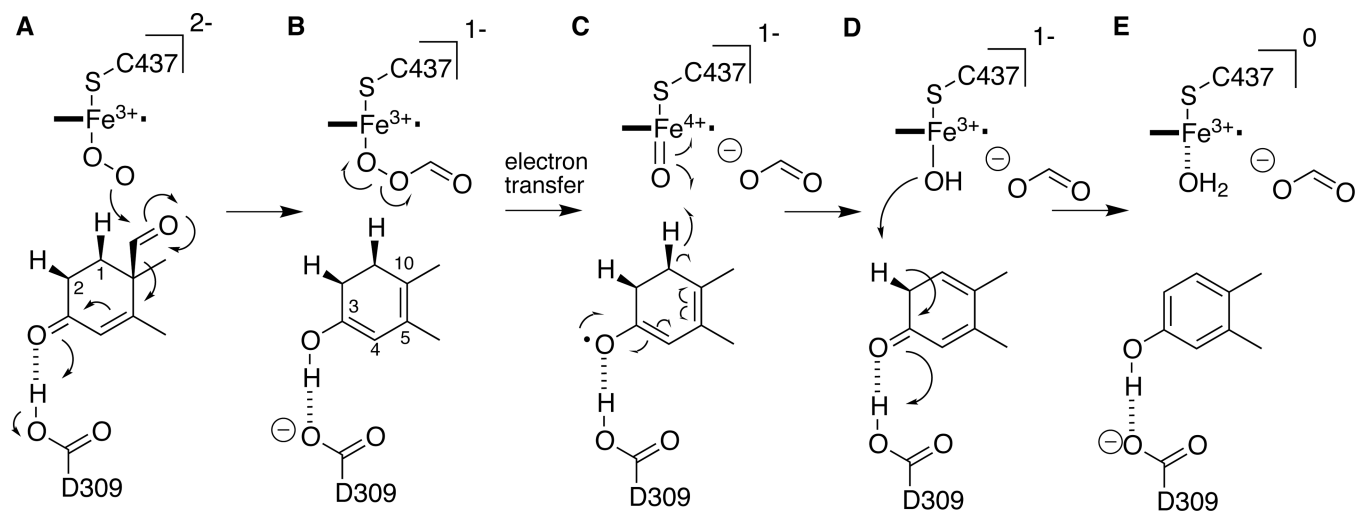
**Figure 5.**

Relative B3LYP/B1:CHARMM22 energetics and structures of intermediates and transition states in the stepwise, OO-cleavage initiated aromatization pathway nascent from the peroxyhemiacetal. Single-point energies at the B3LYP/B2:CHARMM22 and PBE0/B2:CHARMM22 levels of theory are represented in parentheses and italics, respectively. Energies and distances are reported in kcal/mol and Angstroms.





Scheme 1.

**Scheme 2.**